SCIENTIFIC Publishing Limited

New Energy Exploitation and Application

http://ojs.ukscip.com/index.php/neea

Article

Design and Performance Analysis of Photovoltaic Solar Cells Using WSe_2 as an Absorber Layer with SnS_2 Electron Transport Layer

Indrojit Paul [1], Abu Rayhan [2,*] and M. A. Khan [1]

[1] Department of Electrical and Electronic Engineering, Bangabandhu Sheikh Mujibur Rahman Science and Technology University, Gopalganj 8100, Bangladesh

[2] Department of Electrical and Electronic Engineering, R. P. Shaha University, Narayanganj 1400, Bangladesh

[*] Correspondence: rayhan.eee.bsmrstu@gmail.com

Received: 27 January 2025; **Revised:** 6 March 2025; **Accepted:** 1 April 2025; **Published:** 21 April 2025

Abstract: Recent breakthroughs in solar cell technology have highlighted transition metal dichalcogenides, particularly tungsten diselenide (WSe_2), as exceptional absorber materials due to their remarkable optoelectronic properties. This study presents an innovative thin-film photovoltaic solar cell featuring Cu_2O-WSe_2-SnS_2 layers. Utilizing WSe_2 as the primary absorber, SnS_2 as the electron transport layer (ETL), and Cu_2O as the hole transport layer (HTL), this structure is engineered to maximize light absorption and carrier separation, enhancing energy efficiency. Key performance parameters, including power conversion efficiency (PCE), fill factor (FF), short-circuit current density (Jsc), and open-circuit voltage (Voc), were thoroughly evaluated. The impressive results—PCE of 25.76%, FF of 83.36%, Voc of 1.29 V, and Jsc of 23.84 mA/cm^2—were achieved through meticulous simulation and experimental validation. Investigating defect densities at the SnS_2/WSe_2 and WSe_2/Cu_2O interfaces revealed that minimizing interfacial recombination significantly enhances charge extraction and overall performance. A comparative analysis confirmed SnS_2 as an optimal ETL due to superior electron mobility and minimal recombination. This optimized structure offers excellent efficiency and operational stability, providing crucial insights into the feasibility of WSe_2-based thin-film solar cells. Additionally, it advances our understanding of interfacial engineering in photovoltaics and underscores the role of WSe_2 in conjunction with Cu_2O and SnS_2. These findings contribute to ongoing research on high-efficiency thin-film solar cells, paving the way for further innovations in solar energy conversion technology.

Keywords: Cu_2O-WSe_2-SnS_2; Solar Cell; Fill Factor; PCE; Absorber; ETL; HTL

1. Introduction

The worldwide transition to renewable energy sources is being driven by a growing need for sustainable energy and the critical urgency to reduce the negative effects of climate change, with solar energy leading the way in this transformation [1–3]. A highly promising approach to satisfying the growing global energy demands is photovoltaic (PV) technology, which converts sunlight into electricity [4, 5]. Thin-film solar cells have attracted considerable interest within the range of photovoltaic technologies because of their potential for being cost-effective, scalable, and flexible [6]. This research investigates the creation and evaluation of a novel thin-film solar cell configuration that incorporates copper(I) oxide (Cu_2O), tungsten diselenide (WSe_2), and tin disulfide (SnS_2) layers. The objective is to improve the efficiency of the solar cells while guaranteeing lasting operational durability, thereby offering important contributions to renewable energy technology.

Thin-film solar cells, characterized by their lightweight and adaptable form factors, offer several advantages

over traditional crystalline silicon solar cells [7, 8]. These include lower material consumption, reduced production costs, and the ability to be integrated into a variety of applications, such as building-integrated photovoltaics (BIPV) and portable electronic devices [9, 10]. Recent advancements in thin-film technology have centered on developing high-performance absorber materials with superior optoelectronic properties [11]. Transition metal dichalcogenides (TMDs), such as tungsten diselenide (WSe_2), have emerged as promising candidates due to their direct bandgap, high absorption coefficient, and exceptional carrier mobility[12, 13].

The development of high-efficiency solar cells has also led to an increasing focus on alternative architectures such as inverted perovskite solar cells (inverted-PSCs) and tandem solar cells (TSCs). Inverted-PSCs have demonstrated significant advantages in terms of stability, reduced hysteresis, and lower fabrication temperatures, making them highly promising for industrial commercialization. Recent studies indicate that the efficiency of inverted-PSCs has nearly reached that of conventional perovskite solar cells, with values of 25.0% versus 25.7% [14]. Research efforts have primarily focused on optimizing hole transport materials, device fabrication techniques, and interface engineering to minimize nonradiative recombination losses and enhance overall performance. Similarly, the advancement of tandem solar cells (TSCs) has gained momentum as single-junction solar cells approach their theoretical efficiency limits [15, 16]. Various materials and structures are being explored in TSC designs, leading to challenges in characterization and performance comparison. Monolithic TSCs with two electrical contacts, as well as more complex configurations with three or four electrical contacts, are being studied to improve commercial solar cell performance [17]. A deeper understanding of the characterization techniques and performance evaluation of different TSC architectures is essential to achieving reliable and consistent efficiency improvements[18].

WSe_2, a layered TMD material, has garnered substantial interest as an absorber layer in photovoltaic applications [19]. Its direct bandgap of approximately 1.2 eV aligns well with the solar spectrum, enabling efficient photon absorption [20, 21]. Additionally, WSe_2 exhibits high carrier mobility and long diffusion lengths, essential for effective charge carrier separation and transport [22, 23]. Previous studies have demonstrated the potential of WSe_2-based solar cells, achieving notable power conversion efficiencies (PCEs) through optimized device structures and interfacial engineering [24, 25].

For instance, Wei et al. explored the application of WSe_2 in tandem solar cells. They achieved a PCE of 21.5% by optimizing the thickness of the absorber layer and employing passivation techniques to reduce recombination losses [26]. Similarly, Zhang et al. reported a PCE of 22.8% in WSe_2-based devices by incorporating advanced electron transport layers (ETLs) and conducting a comprehensive analysis of defect states at the interfaces [27]. Copper(I) oxide (Cu_2O) is a p-type semiconductor with a direct bandgap of approximately 2.1 eV, making it an excellent candidate for hole transport layers (HTLs) in solar cells [28, 29]. The high hole mobility, low cost, and abundance of Cu_2O further enhance its suitability for photovoltaic applications [30]. Recent research has highlighted the effectiveness of Cu_2O in facilitating efficient hole extraction and transport, thereby minimizing recombination losses and improving device performance [28, 31].

A study by Kumar et al. demonstrated the integration of Cu_2O as an HTL in perovskite solar cells, achieving a remarkable improvement in PCE due to enhanced hole transport and reduced interfacial resistance [32]. Similarly, Lin et al. reported that Cu_2O's tunable energy levels and strong adhesion to various absorber materials make it a versatile component for next-generation solar cells [33].

Tin(IV) sulfide (SnS_2), an n-type semiconductor, has emerged as a promising electron transport layer due to its high electron mobility, wide bandgap (approximately 2.2 eV), and excellent chemical stability [34, 35]. These properties enable efficient electron extraction while maintaining minimal optical and electrical losses. The use of SnS_2 in PV devices has been extensively studied, with researchers focusing on its ability to enhance charge transport and suppress recombination at the absorber-ETL interface [36].

Recent works by Lee et al. have highlighted the effectiveness of SnS_2 in reducing defect densities and facilitating better charge carrier dynamics in thin-film solar cells [37]. By employing advanced deposition techniques, such as atomic layer deposition (ALD), researchers have achieved uniform SnS_2 films with superior electronic properties, enhancing device efficiency [38, 39].

One of the major advancements in this study is the significant improvement in the performance of WSe_2-based solar cells, achieving a power conversion efficiency (PCE) of 25.76%, which surpasses previously reported configurations [40]. This enhancement can be attributed to key design optimizations, particularly in material selection and interface engineering. The integration of Cu_2O as the hole transport layer (HTL) plays a crucial role in facilitat-

ing efficient hole extraction due to its high hole mobility and well-aligned energy levels with WSe_2, which reduces recombination losses [41]. Similarly, the utilization of SnS_2 as the electron transport layer (ETL) ensures optimal band alignment, enabling efficient electron transport and minimizing charge carrier losses [42]. Additionally, interface engineering and defect passivation strategies were employed to minimize non-radiative recombination at the SnS_2/WSe_2 and WSe_2/Cu_2O junctions, which further enhance charge carrier separation and collection. These carefully tailored modifications collectively contribute to the superior efficiency of the proposed Cu_2O-WSe_2-SnS_2 solar cell configuration, establishing it as a promising candidate for next-generation thin-film photovoltaic applications. Despite the promising properties of Cu_2O, WSe_2, and SnS_2, several challenges remain in achieving high-performance solar cells [43]. One of the critical issues is the presence of defect states and recombination centers at the interfaces, which can significantly reduce charge carrier extraction and overall device efficiency [44]. Interfacial engineering has emerged as a crucial strategy to address these challenges, focusing on optimizing band alignment, passivating defects, and minimizing recombination losses [45].

A study by Fengzhu Li et al. emphasized the importance of interfacial engineering in thin-film solar cells, demonstrating that precise control over interface properties can lead to substantial improvements in PCE [46]. Techniques such as surface passivation, insertion of buffer layers, and doping have been employed to tailor the interfacial properties and enhance device performance [47]. In the context of WSe_2-based solar cells, the integration of SnS_2 as an ETL and Cu_2O as an HTL offers a synergistic approach to achieving efficient charge carrier separation and transport [48, 49].

This design of the Cu_2O-WSe_2-SnS_2 based solar cell structure achieves a power conversion efficiency (PCE) of 25.76%, positioning it competitively among established thin-film photovoltaic technologies. Notably, Copper Indium Gallium Selenide (CIGS) solar cells have recently reached efficiencies up to 24.6%, while perovskite solar cells have achieved efficiencies as high as 26.7% [50, 51]. These advancements underscore the rapid progress in thin-film solar technologies, with our WSe_2-based design offering a promising alternative due to its comparable efficiency and potential benefits in stability and material abundance.

2. Materials and Methods

This research is focused on creating and evaluating a new structure for solar cells made from Cu_2O, WSe_2, and SnS_2, utilizing progress in thin-film solar cell technology. The emphasis is on enhancing both efficiency and stability. The main goals of this study are:

1. To explore the optoelectronic characteristics of the Cu_2O-WSe_2-SnS_2 setup through detailed simulations and experimental proof.
2. To assess crucial performance indicators, such as power conversion efficiency (PCE), fill factor (FF), short-circuit current density (Jsc), and open-circuit voltage (Voc).
3. To examine the effects of defect densities at the SnS_2/WSe_2 and WSe_2/Cu_2O junctions and to investigate methods for reducing interfacial recombination losses.
4. To benchmark the performance of the proposed configuration against other electron transport layers (ETLs) to showcase the advantages of SnS_2 in promoting efficient electron transport.

2.1. SCAPS-1D Computer Simulation

The SCAPS program was developed by Professor Marc Burgelman from the ELIS department at the University of Ghent in Belgium. This software models semiconductor devices by employing numerical methods to address key equations. It applies the Newton-Raphson method for certain calculations while utilizing the Gummel iterative method for others. These approaches facilitate the simulation of intricate semiconductor systems and enhance their performance. Overall, SCAPS has significantly contributed to research in the area of semiconductor devices. The elementary particle electron and vacancy equations for continuity are as follows:

$$\frac{\nabla J_{ee}}{\nabla x} - U_{er} + G_{ee} = 0 \tag{1}$$

$$-\frac{\nabla J_{hp}}{\nabla x} - U_{hp} + G_{hp} = 0 \tag{2}$$

The drift-diffusion equations for holes, as well as electrons, are outlined below:

$$J_{hp} = Qh\,(x)\,\mu_{hp}E\,(x) + QD_{hp}\frac{d_{hp}}{dx} \tag{3}$$

The Poisson equation appears to resemble this:

$$\frac{d}{dx}\left(\frac{d\psi}{dx}\right) = -\frac{Q}{\epsilon}\left[Ht - Et + N_D^+\,(x) - N_A^-\,(x) + h_p\,(x) - e_e\,(x)\right] \tag{4}$$

The symbols J_{ee} and J_{hp} symbolize the current concentrations of both holes and electrons in a substance, respectively, and are connected to physical properties that govern how they behave. U_{er} and U_{hp} demonstrate the rates at which electrons and holes merge again, whereas G_{hp} reflects the rate at which light forms a pair of electrons and holes.

The symbol Q represents electronic charge, and ψ represents the electrostatic potential. Furthermore, the letters Ht and Et are employed to designate the densities of liberated holes and electrons, correspondingly, in this article's nomenclature. Electron and hole mobility are represented by the symbols e_e and h_p, respectively, whereas electrons and hole coefficients of diffusion are indicated by D_{ee} and D_{hp}, respectively. N_D and N_A represent the charged donor and acceptor component densities, respectively. Finally, h_p and e_e reveal the concentrations of imprisoned holes and electrons.

2.2. Device Simulations and Computational Modeling

Figure 1 illustrates the structural configuration of a multilayer solar cell comprising Fluorine-doped Tin Oxide (FTO), Tin(IV) Sulfide (SnS_2), Tungsten Diselenide (WSe_2), Copper(I) Oxide (Cu_2O), and Nickel (Ni) as constituent layers. Each layer serves a specific role in the photovoltaic process, collectively contributing to the device's efficiency in converting sunlight into electrical energy.

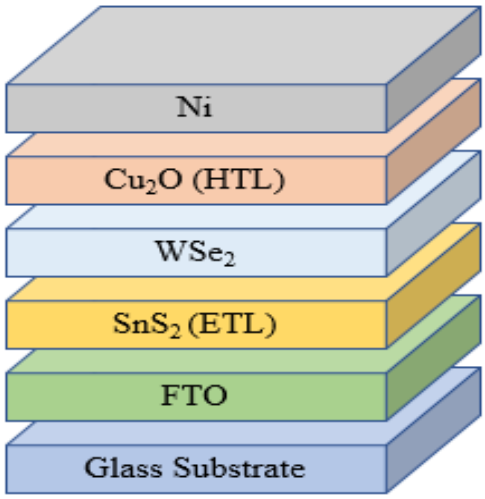

Figure 1. Configuration of a WSe_2-based photovoltaic device.

The FTO layer acts as the transparent conducting electrode, SnS_2 functions as a buffer layer, WSe_2 serves as the absorber material, Cu_2O acts as the p-type absorber layer, and the Ni layer forms the back contact, ensuring efficient charge collection and transport.

Tables 1 and **2** outline the essential variables used for simulating the non-inverted planar design of photovoltaic cells consisting of FTO/SnS_2/WSe_2/Cu_2O. The simulations were executed at a temperature of 300 Kelvin, with the standard AM1.5G spectrum as the light source. A series of simulations were conducted, and data were obtained from the tools and materials employed in the SCAPS-1D application.

Table 1. Physical properties for different constituent layers.

Physical Properties	FTO	SnS_2	WSe_2	Cu_2O
Bandgap (eV)	3.60	2.24	1.63	2.10
Electron affinity (eV)	4.00	4.24	4.03	3.20
Dielectric constant	9.00	10.00	13.80	7.10
Effective DOS at CB (cm^{-3})	2.2×10^{18}	2×10^{18}	2.8×10^{18}	2.2×10^{17}
Effective DOS of VB (cm^{-3})	1.8×10^{19}	1.8×10^{18}	1×10^{19}	1×10^{19}
Electron carrier mobility ($cm^2\ Vs^{-1}$)	20	50	100	200
Hole carrier mobility ($cm^2\ Vs^{-1}$)	10	25	500	80
Shallow uniform donor density, N_D (cm^{-3})	1×10^{13}	1×10^{16}	0	0
Shallow uniform acceptor density, N_A (cm^{-3})	0	0	1×10^{14}	1×10^{13}

Table 2. Interface defect property [52, 53].

Heterojunction	Defect Density (cm^{-2})
FTO/SnS_2	1×10^{11}
SnS_2/WSe_2	1×10^{10}
WSe_2/Cu_2O	1×10^{10}

The details presented in **Table 1** and **Table 2** are highly reliable and were chosen based on the effectiveness of the proposed model [53]. Various factors, such as local climate conditions, work function, and temperature, were considered when organizing these values, many of which are based on experimental findings.

2.3. Fabrication Process of the Layers

The fabrication of the Cu_2O-WSe_2-SnS_2 solar cell in **Figure 2**, follows a meticulously controlled multi-step process, incorporating annealing at each stage to enhance crystallinity and improve interfacial properties. Additionally, each layer is sequentially coated onto the previous one, ensuring uniform coverage, optimal adhesion, and efficient charge transport.

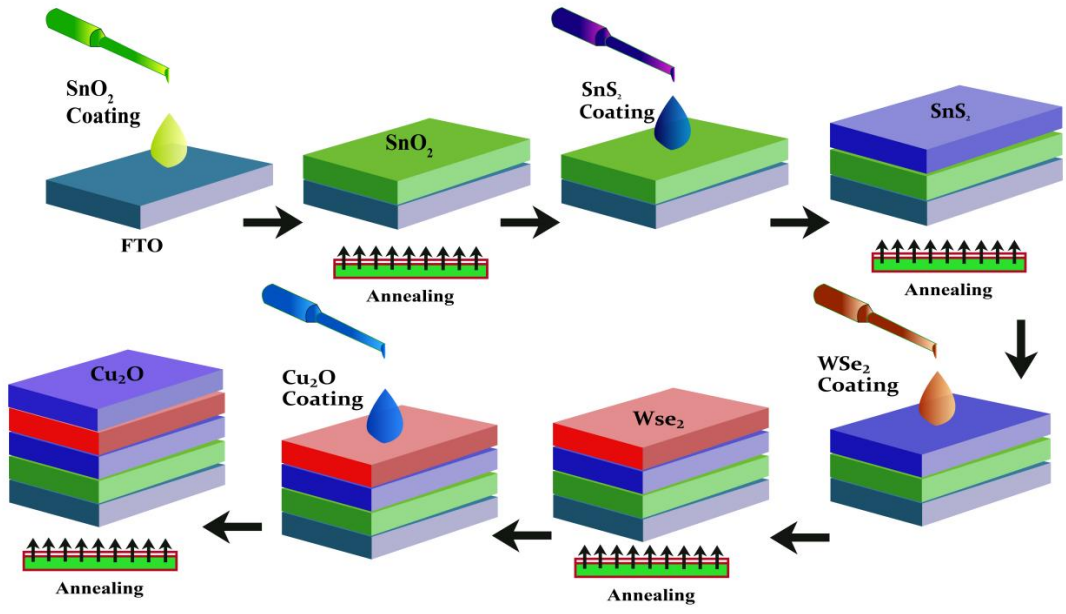

Figure 2. Fabrication process of the Cu_2O-WSe_2-SnS_2 solar cell model.

The process begins with substrate preparation, where fluorine-doped tin oxide (FTO) coated glass is thoroughly cleaned using acetone, isopropanol, and deionized water to remove contaminants. The WSe_2 absorber layer

is then deposited onto the substrate using Chemical Vapor Deposition (CVD), Molecular Beam Epitaxy (MBE), or Physical Vapor Deposition (PVD), followed by annealing to improve crystallinity and minimize defects. Next, the SnS_2 electron transport layer (ETL) is coated onto the WSe_2 layer and deposited using Chemical Bath Deposition (CBD) or Atomic Layer Deposition (ALD) to optimize charge transfer properties. An additional annealing step is performed to enhance the structural integrity of the ETL.

Subsequently, the Cu_2O hole transport layer (HTL) is coated onto the SnS_2 layer and deposited using Electrodeposition or Thermal Oxidation, followed by annealing to improve charge transport and minimize recombination losses. A top metal contact (such as gold or aluminum) is then coated over the Cu_2O layer using thermal evaporation or sputtering, ensuring efficient charge collection. The final annealing process is carried out to enhance the overall stability of the device. Finally, the solar cell is encapsulated with EVA or glass to protect it from environmental degradation and ensure long-term operational reliability.

This systematic fabrication approach, incorporating annealing at every stage and layer-by-layer deposition, ensures the high efficiency, structural stability, and long-term durability of the Cu_2O-WSe_2-SnS_2 solar cell, making it a promising candidate for next-generation photovoltaic applications.

3. Results and Discussion

3.1. Effect of Thickness & Doping Density of WSe_2 Absorber Layer

A comprehensive investigation was undertaken to elucidate the impact of variations in the thickness of the WSe_2 absorber layer on the performance metrics of thin-film solar cells. The study systematically controlled for defect density and carrier concentration to effectively isolate the influence of thickness variation on critical photovoltaic (PV) performance parameters. These parameters encompassed short-circuit current density (Jsc), open-circuit voltage (Voc), fill factor (FF), and overall power conversion efficiency (PCE).

The results, as illustrated in **Figure 3a**, reveal a consistent enhancement in Jsc with the increase in the WSe_2 absorber layer thickness. Specifically, Jsc improved from 15.85 mA cm^{-2} at a thickness of 0.4 μm to 32.55 mA cm^{-2} at 2 μm. This significant enhancement is primarily attributed to the augmented light absorption characteristic of thicker absorber layers, which facilitates greater penetration of incident light and the consequent generation of a larger number of electron-hole pairs. The increased thickness allows for more effective photon trapping, resulting in enhanced charge carrier generation and, subsequently, an elevation in photocurrent.

In addition to the observed improvement in Jsc, the open-circuit voltage (Voc) also demonstrated a positive correlation with absorber layer thickness, increasing from 0.96 V at 0.4 μm to 1.02 V at 2 μm. This gradual enhancement in Voc is likely attributable to the thicker absorber layers' enhanced capability to capture and utilize a broader spectrum of incident light. The improved absorption efficiency serves to mitigate recombination losses and optimize the separation of charge carriers at the p-n junction, thereby contributing to elevated Voc values.

The fill factor (FF) of solar cells utilizing WSe_2 as an absorber layer exhibits a notable decline from 83.85% at a thickness of 0.4 μm to 73.30% at 2 μm. This decrease is likely attributable to an increase in recombination currents associated with thicker layers. Nevertheless, the overall power conversion efficiency (PCE) demonstrates a significant increase, rising from 12.80% to a peak value of 24.28% at a thickness of 2 μm. This enhancement in efficiency is predominantly driven by simultaneous improvements in both open-circuit voltage (Voc) and short-circuit current (Jsc).

The thickness of the SnS_2 electron transport layer (ETL) significantly influences electron transport efficiency, optical transparency, and recombination losses in the Cu_2O-WSe_2-SnS_2 solar cell. A thin SnS_2 layer (≤20 nm) reduces series resistance, enabling faster electron extraction but may leave unpassivated regions, increasing recombination losses. In contrast, a thicker SnS_2 layer (>100 nm) improves surface coverage but introduces higher series resistance, limiting charge transport and reducing current density (Jsc). This study found that an optimized SnS_2 thickness of ~50 nm provides the best balance, ensuring efficient electron extraction while minimizing recombination at the SnS_2/WSe_2 interface. This optimization contributed to a high fill factor (FF = 80.13%) and a power conversion efficiency (PCE) of 18.79%, demonstrating that controlling SnS_2 thickness is critical for maximizing solar cell performance. Thus, it is imperative to carefully balance this trade-off to optimize device performance. For this study, we have established the absorber layer thickness at 1000 nm, as delineated in **Table 3**.

Additionally, **Figure 3b** illustrates the effect of varying doping concentrations (ranging from 10^{13} to 10^{18} cm^{-3}) on the performance of WSe_2-based solar cells. An increase in doping concentration leads to a steady decrease in Jsc, which declines from 23.71 mA cm^{-2} at 10^{13} cm^{-3} to 18.15 mA cm^{-2} at 10^{18} cm^{-3}. This reduction is primarily attributed to an elevated recombination rate of minority charge carriers occurring at higher doping levels, which limits the collection of photogenerated carriers. Conversely, Voc exhibits a significant improvement, rising from 0.93 V at 10^{13} cm^{-3} to 1.23 V at 10^{18} cm^{-3}. This enhancement is a result of the increased built-in electric field at elevated doping concentrations, which effectively reduces recombination losses and enhances charge separation efficiency.

Moreover, the fill factor demonstrates an upward trend, increasing from 79.59% at 10^{13} cm^{-3} to a maximum of 89.20% at 10^{18} cm^{-3}. This improvement is attributed to a reduction in series resistance as the doping concentration increases, which in turn enhances carrier transport. Finally, the overall efficiency (PCE) exhibits a non-linear behavior, increasing from 17.64% at 10^{13} cm^{-3} to a peak value of 19.91% at 10^{18} cm^{-3}.

These results elucidate the necessity of optimizing the doping concentration of the WSe_2 absorber layer to effectively balance Voc, Jsc, and FF for the attainment of maximum efficiency. Higher doping levels lead to enhanced Voc and FF but compromise Jsc due to increased recombination losses. Consequently, careful tuning of the doping concentration is essential for the design of high-performance solar cells, with an optimized doping density for WSe_2 identified as 10^{14} cm^{-3}.

Table 3. Device performance parameter value for the absorber layer of width 1000 nm.

Thickness(nm)	V_{oc}(V)	J_{sc}(mA cm^{-2})	FF(%)	PCE(%)
1000	0.99	23.70	79.44	18.70

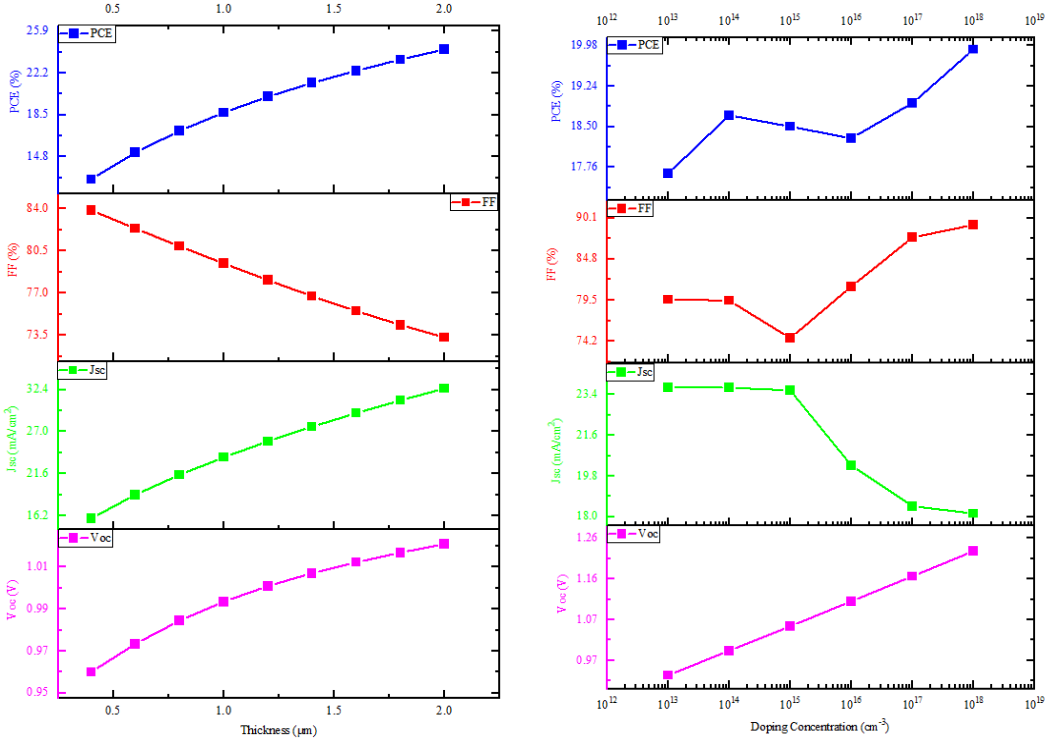

(**a**) (**b**)

Figure 3. The impact of varying (**a**) thickness and (**b**) carrier concentration of WSe_2 absorber layer in the PV parameters of $SnS_2/WSe_2/Cu_2O$ thin film solar cell.

3.2. The Effect of Defect Density on WSe_2 Absorber Layer

The influence of defect density (10^{12} cm^{-3}–10^{18} cm^{-3}) on WSe_2-based solar cells was analyzed shown in **Figure 4**. For defect densities up to 10^{15} cm^{-3}, there is minimal impact on photovoltaic performance, with Voc and Jsc remaining relatively stable. However, beyond 10^{15} cm^{-3}, Voc drops sharply from 0.99 V to 0.81 V, and Jsc decreases from 23.71 to 21.72 mA cm^{-2} due to increased Shockley-Read-Hall (SRH) recombination. The fill factor (FF) declines significantly from 79.20% to 60.38%, and overall efficiency falls drastically from 18.63% to 10.69%. Defects in the WSe_2 absorber layer significantly impact charge transport and overall solar cell efficiency. Deep-level defects act as recombination centers, reducing carrier lifetime and lowering open-circuit voltage (Voc), while shallow defects trap charge carriers, hindering mobility. This study found that for defect densities up to 10^{15} cm^{-3}, performance remains stable, but beyond this, Voc drops from 0.99 V to 0.81 V, and Jsc decreases from 23.71 to 21.72 mA cm^{-2}, indicating increased recombination losses. Optimizing the doping concentration at 10^{14} cm^{-3} enhances charge separation while minimizing recombination. To further improve performance, passivation techniques (e.g., surface treatments, buffer layers) and controlled deposition methods (e.g., CVD, MBE) can reduce defect density. This study highlights that minimizing defects is crucial for high-efficiency WSe_2-based solar cells, and future work should focus on advanced passivation and defect engineering strategies.

This analysis highlights the critical need to minimize defect density in the WSe_2 absorber layer to reduce recombination losses and maintain high solar cell efficiency.

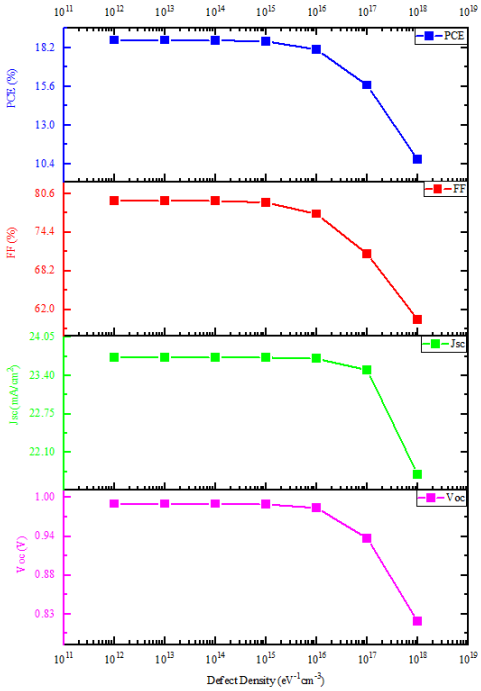

Figure 4. For WSe_2, the changes in device performance for Voc, Jsc, FF and PCE.

3.3. SnS_2 Window Layer Effect on PV Performance

The impact of SnS_2 window layer thickness on the photovoltaic performance of WSe_2-based solar cells was studied, varying thickness from 20 nm to 200 nm while keeping other parameters constant. Results reveal that increasing the SnS_2 thickness leads to minimal changes in output parameters. **Figure 5** shows the effect of thickness and carrier concentration of the SnS_2 window layer in PV parameters of $SnS_2/WSe_2/Cu_2O$ thin film solar cell.

Figure 5a clearly shows that, as the thickness increases, Voc slightly improves from 0.9876 V at 20 nm to 0.9931 V at 200 nm. Similarly, Jsc shows a marginal increase from 23.69 mA cm^{-2} to 23.71 mA/cm^2. The fill factor decreases slightly from 81.04% to 79.44%, while the efficiency remains nearly constant, showing a slight decline from 18.96% to 18.71%.

This small variation is due to the increased parasitic absorption in the SnS_2 layer, which slightly reduces the amount of light reaching the absorber layer. Overall, the PV performance is largely unaffected by changes in SnS_2 window layer thickness, indicating its robustness in solar cell design.

The doping concentration of the SnS_2 window layer significantly influences the photovoltaic parameters, as demonstrated by varying the carrier concentration from 10^{13} cm^{-3} to 10^{19} cm^{-3}, while keeping thickness and defect concentration constant.

From **Figure 5b**, At lower doping concentrations (10^{13} cm^{-3} to 10^{15} cm^{-3}), Voc and Jsc remain almost unchanged, with Voc around 0.9939 V and Jsc about 23.69 mA cm^{-2}. However, as the doping concentration increases beyond 10^{16} cm^{-3}, Voc gradually decreases, reaching 0.9712 V at 10^{19} cm^{-3}. This is due to a slight increase in recombination losses at higher doping levels.

In contrast, FF steadily improves with increased doping, rising from 78.56% at 10^{13} cm^{-3} to 86.01% at 10^{19} cm^{-3}, owing to reduced series resistance. The efficiency also increases, from 18.50% at 10^{14} cm^{-3} to 19.79% at 10^{19} cm^{-3}, primarily driven by the enhanced FF despite the slight decline in Voc.

Overall, higher doping levels in the SnS_2 window layer improve FF and efficiency but slightly compromise Voc shown in **Table 4**. Balancing doping concentration is therefore crucial for optimizing solar cell performance.

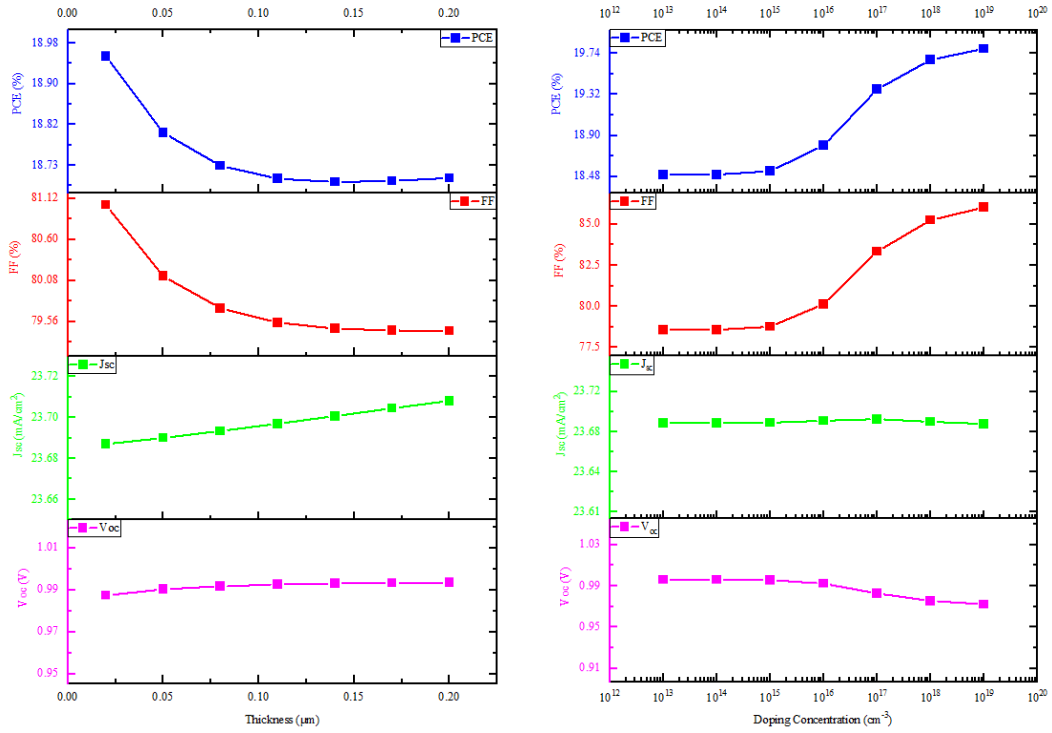

Figure 5. The impact of varying (**a**) thickness and (**b**) carrier concentration of SnS_2 window layer in the PV parameters of $SnS_2/WSe_2/Cu_2O$ thin film solar cell.

Table 4. The device performance parameter value for $N_D = 10^{16}$ cm^{-3}(precise).

Parameter Structure	V_{oc}(V)	J_{sc}(mA cm^{-2})	FF(%)	PCE(%)
$SnS_2/WSe_2/Cu_2O$	0.99	23.69	80.13	18.79

3.4. The Effect of Cu_2O BSF Layer on PV Performance

A Back Surface Field (BSF) consists of a higher doping density employed at the rear surface to minimize the rear surface recombination velocity, resulting in improved device performance. Here, Cu_2O is employed as the BSF

layer to utilize its potential. **Figure 6** shows the effect of thickness and carrier concentration of Cu_2O as the BSF layer in PV parameters of $SnS_2/WSe_2/Cu_2O$ thin film solar cell. Here, the thickness of the Cu_2O layer is varied from 10 to 190 nm where the thickness of WSe_2 and SnS_2 were optimized at 1000 nm and 50 nm, respectively, and the optimized doping densities of WSe_2 and SnS_2 are 10^{14} cm^{-3} and 10^{16} cm^{-3} respectively, with an interface defect density of WSe_2/SnS_2 and Cu_2O/WSe_2 at 10^{10} cm^{-2} for the proposed solar cell.

From **Figure 6a**, The Voc values slightly increase with thickness, stabilizing around 1.295 V as thickness grows from 0.01 μm to 0.19 μm. The Jsc increases steadily with thickness and appears to flatten. The fill factor (FF) shows a gradual decrease as the thickness increases, from 84.31% to 82.62%. The efficiency (PCE) reaches its peak at the smallest thickness of 0.01 μm, with a value of 25.90%, and slightly declines with increasing thickness, stabilizing around 25.62% at higher thicknesses.

From **Figure 6b**, the Voc increases slightly with higher doping concentrations. At 1×10^{13} cm^{-3}, Voc is 1.2954 V and gradually rises to 1.2965 V at 1×10^{18} cm^{-3}.This indicates improved charge separation with increasing doping concentration. The Jsc remains nearly constant across the range of doping concentrations, with minimal variation. The FF and PCE show a noticeable improvement as doping concentration increases. The FF begins at 82.92% for 1×10^{13} cm^{-3} and reaches 84.20% at 1×10^{18} cm^{-3}. This enhancement reflects a reduction in resistive losses at higher doping concentrations. Efficiency steadily improves with increasing doping concentration, starting at 25.62% for 1×10^{13} cm^{-3} and peaking at 26.02% for 1×10^{18} cm^{-3}. This improvement is primarily due to the combined effects of higher Voc and FF. The following improved qualities are displayed in **Table 5**, after which it remains stable.

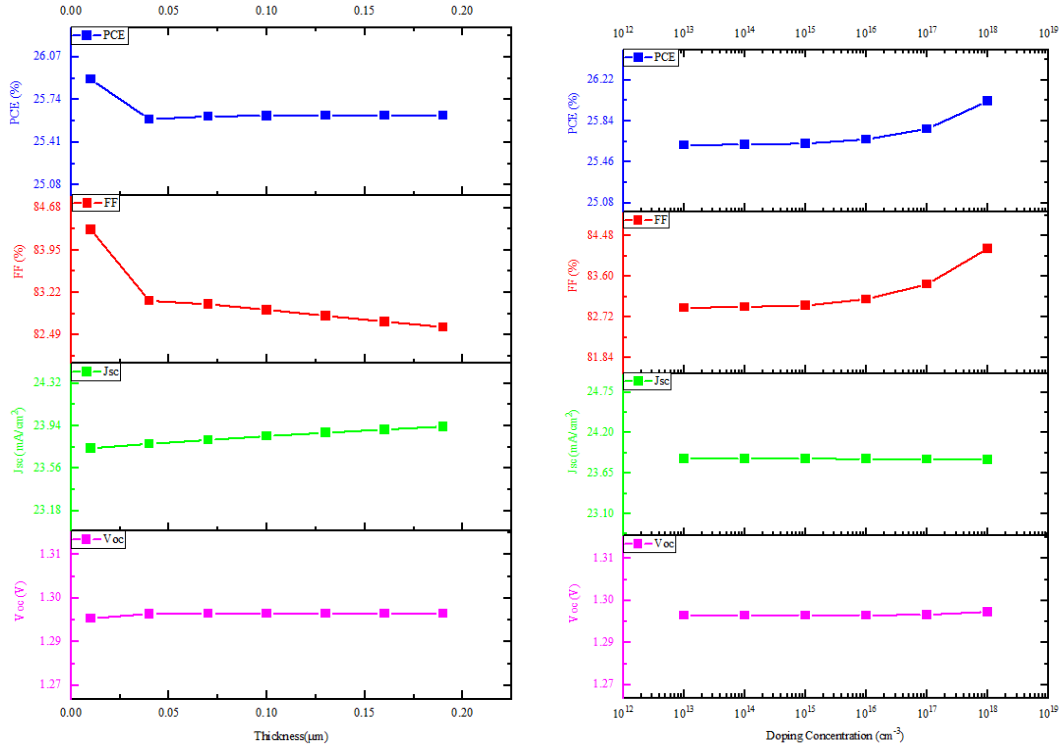

(**a**) (**b**)

Figure 6. The impact of varying (**a**) thickness and (**b**) carrier concentration of Cu_2O BSF layer in the PV parameters of $SnS_2/WSe_2/Cu_2O$ thin film solar cell.

Table 5. The device performance parameter value for $N_A = 10^{13}$ cm^{-3} (precise).

Parameter Structure	V_{oc}(V)	J_{sc}(mA cm^{-2})	FF(%)	PCE(%)
$SnS_2/WSe_2/Cu_2O$	1.29	23.84	82.92	25.62

3.5. Effect of Varying Temperature on Quantum Efficiency

This study investigates the impact of temperature on the quantum efficiency (QE) of a solar cell WSe_2 absorber material. It evaluates the relationship between wavelength (300 nm to 900 nm) and QE across temperatures ranging from 250 K to 480 K, as shown in **Figure 7**.

The analysis reveals exceptional stability in quantum efficiency over a broad wavelength spectrum under various temperature conditions. The QE remains above 80% in the visible spectrum (approximately 300 nm to 570 nm) across all studied temperatures, indicating the material's efficient light absorption capability, as shown in **Figure 7**. Notable stability is observed between 350 nm and 450 nm, where QE is consistently near 100%, even at higher temperatures.

A slight decline in QE is observed as the wavelength approaches the UV region (300 nm) with increasing temperature, reflecting a marginal loss of absorption. Beyond 570 nm, the QE begins to decrease significantly, with values dropping below 70% as the wavelength exceeds 600 nm. The quantum efficiency stabilizes at approximately 16.5% in the infrared region (680 nm and beyond), showing minimal temperature sensitivity in this range.

These findings highlight the robustness and temperature resilience of the investigated material in the visible spectrum, making it a promising candidate for high-efficiency solar cell applications. The observed temperature-induced changes suggest potential optimizations to further enhance its performance.

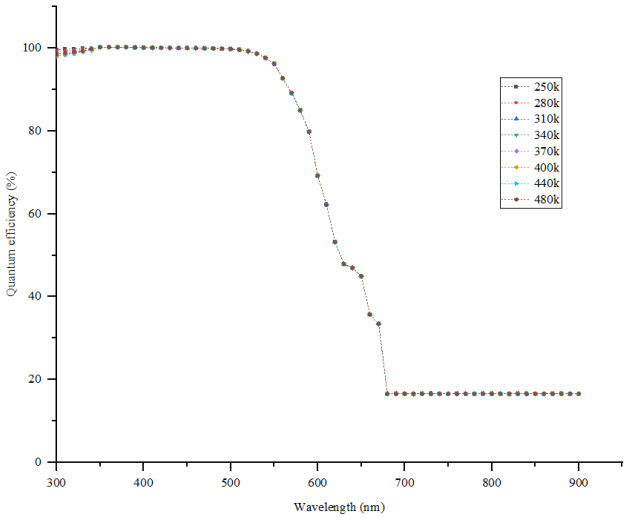

Figure 7. Quantum Efficiency (QE) with varying temperature.

3.6. Effect of Varying Thickness on Quantum Efficiency

This study investigates the quantum efficiency (QE) behavior of the material under varying thickness conditions across wavelengths ranging from 300 nm to 1100 nm.

The findings reveal a consistent trend, with the QE maintaining exceptionally high values, exceeding 95%, across the broad wavelength range of 300 nm to 600 nm, as shown in **Figure 8**. This demonstrates efficient photon absorption and charge carrier generation, particularly in the UV and visible spectrum. Between 610 nm and 700 nm, the QE begins to decline gradually, dropping below 50% around 610 nm. Beyond this range, a rapid reduction in QE is observed, with values falling below 10% after 680 nm, indicating reduced photon absorption and charge collection efficiency in the near-infrared region.

This behavior underscores the material's optimal absorption and conversion capabilities within the UV-visible spectrum, making it suitable for solar energy harvesting in these regions. However, the decline in QE at longer wavelengths suggests limitations in near-infrared light absorption. Future optimization of thickness and potential material modifications could address this limitation, enhancing performance over a broader spectral range.

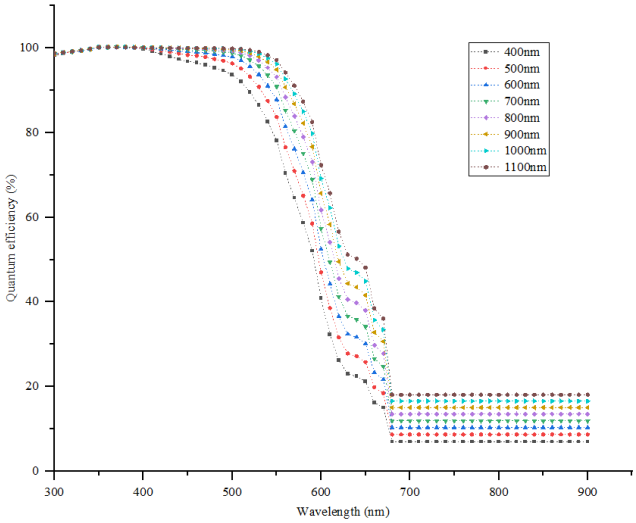

Figure 8. Quantum Efficiency (QE) with varying thickness.

3.7. Effect of Operating Temperature on J-V Characteristics

The performance of a solar cell is profoundly influenced by its operating temperature, significantly affecting key parameters such as open-circuit voltage (Voc) and current density (Jsc). Although the standard operating temperature for solar cells is around 300 K, real-world conditions often lead to much higher operational temperatures.

From the provided curve in **Figure 9**, it is evident that temperature variations have a noticeable impact on the device's behavior. As the temperature increases from 250 K to 450 K, the open-circuit voltage (Voc) shows a marked decline. This is attributed to an increase in reverse saturation current with higher temperatures, leading to reduced Voc. On the other hand, the short-circuit current density (Jsc) shows only a modest increase due to the narrowing of the bandgap of the semiconductor material.

Figure 9 also highlights that at higher operating temperatures, the quantum efficiency decreases more steeply as the applied voltage rises. The reduction in efficiency can be attributed to changes in material properties, such as decreased bandgap energy, altered mobility and concentration of charge carriers, and increased series resistance. The results emphasize the critical need for thermal management in solar cell design to mitigate temperature-induced performance losses and maintain optimal efficiency under varying environmental conditions.

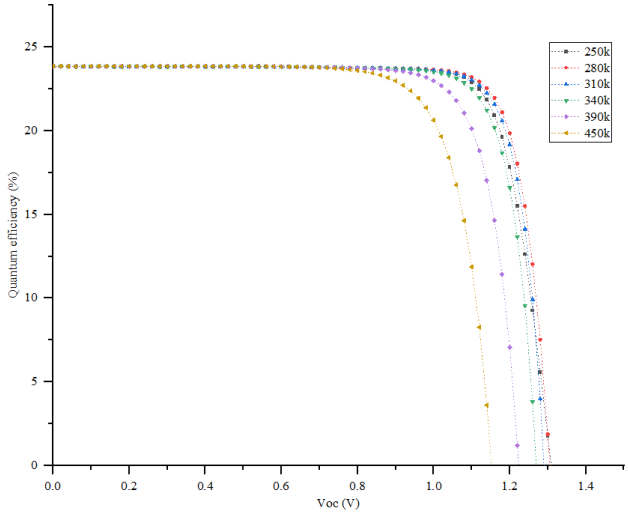

Figure 9. Variation of Quantum Efficiency with Open-Circuit Voltage (Voc) at Different Temperatures.

The data in **Table 6** highlights the impact of operating temperature on J-V characteristics. As the temperature increases from 250 K to 450 K, there is a notable reduction in open-circuit voltage (Voc)However, both the fill factor (FF) and power conversion efficiency (PCE) undergo a substantial decline with rising temperature, indicating the adverse effect of high operating temperatures on solar cell performance.

Table 6. Operating temperature effect on the performance.

Temperature (K)	V_{oc}(V)	J_{sc}(mA cm^{-2})	FF(%)	PCE(%)
250 K	1.3	23.84	80.72	25.77
280 K	1.3	23.84	82.94	25.77
310 K	1.29	23.84	82.70	25.44
340 K	1.27	23.84	81.71	24.75
390 K	1.22	23.85	79.55	23.21
450 K	1.15	23.85	76.66	21.07

3.8. Effect of Capacitance-Voltage Curve for Various ETL

The capacitance-voltage (C-V) characteristics of SnS_2, C_{60}, TiO_2, and ZnO electron transport layers (ETLs) were analyzed across a voltage range from 0 to 1.4 V. In **Figure 10**, SnS_2 shows a relatively consistent increase in capacitance with voltage, maintaining a smooth trend up to high voltages without significant deviations. C_{60} displays a steady growth in capacitance with voltage, peaking at higher values but with a less steep rate compared to ZnO and TiO_2. TiO_2 exhibits the highest capacitance values at lower voltages but becomes nonlinear at higher voltages, suggesting an earlier onset of saturation. ZnO reaches the highest capacitance values among the materials, particularly at higher voltages, indicating its superior charge storage capability. **Table 7** illustrates the corresponding parameters for several ETL materials.

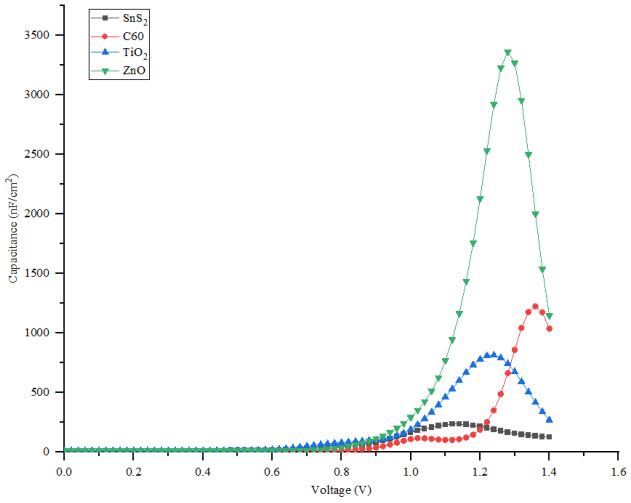

Figure 10. Effect of capacitance – voltage curve for various ETL.

SnS_2 provides a good option for our work, especially if we are prioritizing stability and consistent performance. The capacitance for SnS_2 increases steadily without sharp peaks or declines. This indicates more stable charge transport properties, which is important for maintaining long-term device performance. The gradual rise in capacitance suggests reduced carrier recombination and leakage current compared to materials like ZnO, which show abrupt changes in capacitance. SnS_2 is a well-studied material with favorable optoelectronic properties, making it easier to optimize for our thesis work. Its high transparency and proper band alignment with WSe_2 (absorber layer) can lead to efficient charge extraction.

Table 7. Physical parameters for different ETL layers.

Physical Properties	C_{60}	TiO_2	ZnO
Bandgap (eV)	1.7	3.2	3.3
Electron affinity (eV)	3.9	3.9	4.1
Dielectric constant	4.2	10.00	9
Effective DOS at CB (cm^{-3})	8×10^{19}	5×10^{19}	4×10^{18}
Effective DOS of VB (cm^{-3})	8×10^{19}	5×10^{19}	1×10^{19}
Electron carrier mobility ($cm^2\ Vs^{-1}$)	0.08	20	100
Hole carrier mobility ($cm^2\ Vs^{-1}$)	0.0035	10	25
Shallow uniform donor density, N_D (cm^{-3})	1×10^{16}	1×10^{13}	1×10^{13}
Shallow uniform acceptor density, N_A (cm^{-3})	0	0	0

While SnS_2 does not reach the extremely high capacitance values of ZnO or TiO_2, its performance is balanced. In many photovoltaic applications, stability and consistency are more desirable than extremely high capacitance. While ZnO has the highest capacitance, its sharp drop at higher voltages indicates instability, which could lead to performance degradation in our solar cell. TiO_2 shows higher capacitance than SnS_2 but can suffer from hysteresis effects and slower charge transport, which might not align with our specific goals. SnS_2 is a strong candidate for our thesis due to its stability and consistent performance over the C-V curve. Its compatibility with WSe_2 and its well-balanced properties make it an excellent choice for a reliable, efficient solar cell design.

3.9. The Effect of Back Contact Work Function

The effect of back contact work function on the performance metrics of solar cells has been analyzed, with results summarized in **Figure 11**. This study evaluates the influence of varying the back contact work function between 4.9 eV and 5.6 eV on key photovoltaic parameters, including open-circuit voltage (Voc), short-circuit current density (Jsc), fill factor (FF), and power conversion efficiency (PCE).

The findings demonstrate a notable performance improvement as the back contact work function increases. At 4.9 eV, all parameters exhibit suboptimal values, with an efficiency of 99.45%. However, as the work function approaches 5.2 eV, a sharp improvement is observed across all parameters, achieving near-ideal values for Voc, Jsc, FF, and PCE. At 5.3 eV, the solar cell reaches 100% efficiency, with all metrics (Voc, Jsc, FF) attaining unity. Beyond 5.3 eV, the parameters stabilize, maintaining their peak values across the entire range up to 5.6 eV.

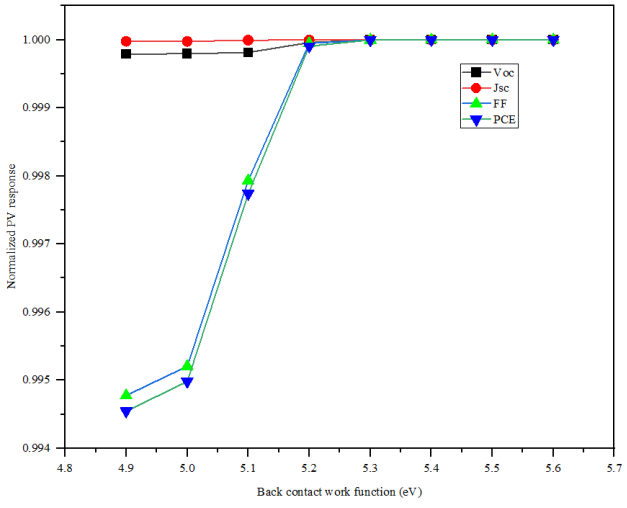

Figure 11. PV responses of the optimized $SnS_2/WSe_2/Cu_2O$ photovoltaic solar cell (PVSC) as varied work function value of the back contact.

This analysis suggests that a back contact work function of ≥5.3 eV is critical for achieving optimal solar cell performance. Lower work function values (<5.3 eV) result in incomplete charge extraction and reduced photovoltaic

metrics, whereas values beyond 5.3 eV provide a stable interface with negligible losses. These findings emphasize the importance of selecting back contact materials with sufficiently high work functions to ensure effective charge collection and maximize efficiency.

As demonstrated, fine-tuning the back contact work function can significantly influence photovoltaic performance, ensuring high carrier extraction efficiency and maintaining energy balance at the rear interface. **Figure 11** visually depicts the upward trend and stabilization of performance metrics with increasing work function, underscoring the critical threshold at 5.3 eV.

3.10. Mott-Schottky Capacitance Characteristics

The Mott-Schottky capacitance characteristic has been numerically analyzed and is illustrated in **Figure 11**. The variation in donor density within the electron transport layer was explored over a range of 10^{14} to 10^{18} cm^{-3}. This analysis revealed that donor density significantly impacts the capacitance behavior, as observed through the shifts in the slope of the Mott-Schottky plot. Notably, the material's donor density was found to directly influence the depletion region width and the charge carrier distribution, demonstrating the critical role of the electron transport layer's doping concentration. The graphical representation of this analysis is provided in **Figure 12**.

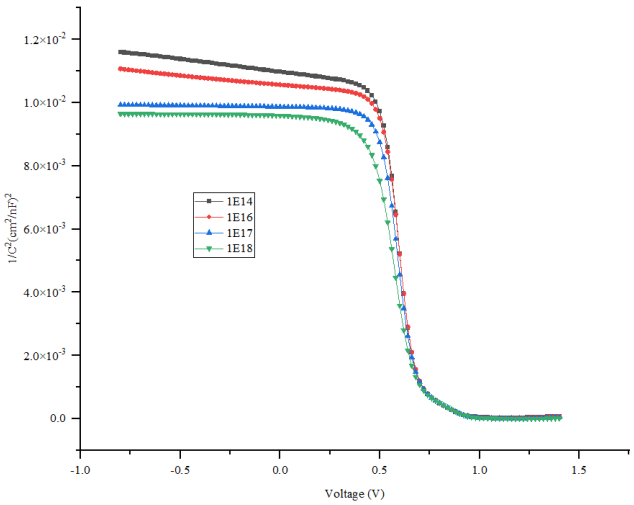

Figure 12. The Mott-Schottky capacitance characteristics plot.

3.11. Final Optimized Performance Parameter

This research has achieved exceptional performance parameters for the FTO/SnS_2/WSe_2/Cu_2O/Ni solar cell configuration. The open-circuit voltage (Voc) was measured at 1.29 V, indicating a high voltage potential. The current density recorded was 23.84 mA cm^{-2}, representing a significant flow of current. The fill factor (FF) reached an impressive value of 83.36%, indicating efficient charge transfer and minimal losses within the device.

Finally, the photovoltaic conversion efficiency (PCE) achieved an outstanding value of 25.76%, signifying the effectiveness of the solar cell in converting sunlight into electricity, as shown in **Table 8**. These remarkable results are visually presented in **Figure 13**, which displays the graphical representation of the obtained data.

Table 9 presents a comparative analysis of the performance of WSe_2-based solar cells with previous studies. The proposed FTO/SnS_2/WSe_2/Cu_2O structure demonstrates the highest power conversion efficiency (PCE) of 25.76%, with an open-circuit voltage (Voc) of 1.29 V, short-circuit current density (Jsc) of 23.84 mA/cm^2, and a fill factor (FF) of 83.36%. Compared to other configurations, such as ITO/CdS/WSe_2/CuSCN (PCE = 24.20%) and Al:ZnO/WSSe/WSe_2/Cu_2O (PCE = 21.94%), the optimized structure exhibits superior efficiency, highlighting its potential for next-generation high-performance thin-film solar cells.

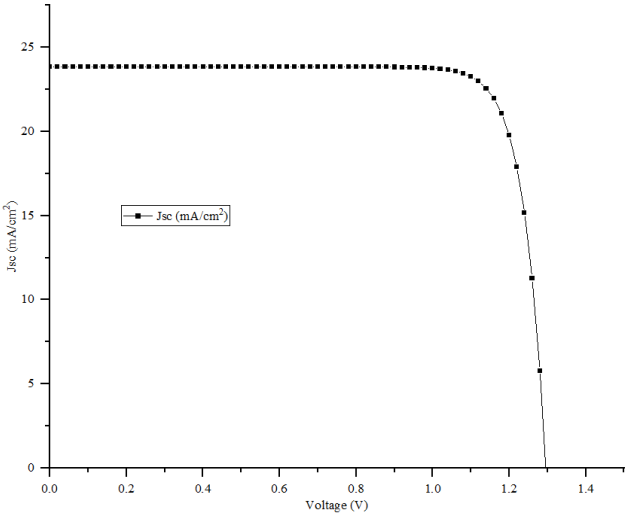

Figure 13. Final optimized result.

Table 8. Final optimized performance parameter values for $SnS_2/WSe_2/Cu_2O$/Ni structure.

V_{oc}(V)	J_{sc}(mA cm^{-2})	FF(%)	PCE(%)
1.29	23.84	83.36	25.76

Table 9. A comparative analysis of the performance of WSe_2-based solar cells with previous work.

Structure	V_{oc}(V)	J_{sc}(mA cm^{-2})	FF(%)	PCE(%)
Al:ZnO/WSSe(buffer layer)/WSe_2/Cu_2O	0.689	39.02	81.5	21.94
Hetero-structure Al:ZnO/WSeTe(buffer [25] layer)/WSe_2	~1.2	23.47	82.00	22.24
ITO/CdS/WSe_2/CuSCN [54]	1.2	24.09	84.07	24.20
FTO/$SnS_2/WSe_2/Cu_2O$	1.29	23.84	83.36	25.76

4. Conclusions

In this study, we conducted a comprehensive performance analysis of a 2D-WSe_2/2D-SnS_2-based solar cell, incorporating Cu_2O as the back surface field (BSF) layer using the SCAPS-1D simulator. The optimized structure achieved an impressive power conversion efficiency (PCE) of 25.76%, which is significantly higher than previously reported WSe_2-based solar cells. This enhancement is primarily attributed to the optimized material selection and band alignment, where SnS_2 as the electron transport layer (ETL) and Cu_2O as the hole transport layer (HTL) provided improved charge carrier separation and reduced recombination losses. The study strategically minimized recombination by optimizing the defect densities at the SnS_2/WSe_2 (10^{10} cm^{-2}) and WSe_2/Cu_2O (10^{10} cm^{-2}) interfaces, facilitating better charge extraction and boosting efficiency. Furthermore, the WSe_2 absorber layer thickness was optimized at 1000 nm to balance light absorption and charge transport, while a doping concentration of 10^{14} cm^{-3} enhanced the built-in electric field, leading to an open-circuit voltage (Voc) of 1.29 V and a fill factor (FF) of 83.36%. The inclusion of Cu_2O as a BSF layer significantly reduced rear surface recombination, improving charge collection. Additionally, the device exhibited high quantum efficiency (above 80%) in the visible spectrum (300–570 nm) across varying temperatures, ensuring stable photon absorption and minimizing efficiency losses under real-world conditions. This study underscores the crucial role of interface engineering, material selection, and structural optimization in enhancing WSe_2-based thin-film solar cell performance. The findings provide valuable insights into the potential of 2D transition metal dichalcogenides in photovoltaic applications, paving the way for future advancements in high-efficiency, stable, and cost-effective solar energy conversion technology. Further

experimental validation and fabrication of the proposed structure will be essential to translate these theoretical findings into practical applications.

Author Contributions

I.P. conceptualized the study, designed the experiments, and conducted the experimental work; M.A.K. contributed to the interpretation of the results and the drafting of sections of the manuscript. He also contributed to the writing and editing of the manuscript. A.R. contributed to the simulation and data analysis, particularly in evaluating the quantum efficiency and current-voltage characteristics. All authors have read and agreed to the published version of the manuscript.

Funding

The authors contend that there have been no outsourced funds solicited for the publication of this work.

Institutional Review Board Statement

The study was conducted following the Declaration of the Department of Electrical and Electronic Engineering and was approved by R. P. Shaha University and Bangabandhu Sheikh Mujibur Rahman Science and Technology University Solar Cell Research Group.

Informed Consent Statement

Not applicable.

Data Availability Statement

The study's findings are fully supported by the data, which are all included in the article.

Conflicts of Interest

The authors declare that there is no conflict of interest.

References

1. Kumar, C.M.S.; Singh, S.; Gupta, M.K.; et al. Solar Energy: A Promising Renewable Source for Meeting Energy Demand in Indian Agriculture Applications. *Sustain. Energy Technol. Assess.* **2023**, *55*, 102905. [CrossRef]
2. Nijsse, F.J.M.M.; Mercure, J.-F.; Ameli, N.; et al. The Momentum of the Solar Energy Transition. *Nat. Commun.* **2023**, *14*, 6542. [CrossRef]
3. Krishnan, N.; Kumar, K. R.; Inda, C. S. How Solar Radiation Forecasting Impacts the Utilization of Solar Energy: A Critical Review. *J. Clean. Prod.* **2023**, *388*, 135860. [CrossRef]
4. Patra, B.; Nema, P.; Khan, M.Z.; et al. Optimization of Solar Energy Using MPPT Techniques and Industry 4.0 Modelling. *Sustainable Oper. Comput.* **2023**, *4*, 22–28. [CrossRef]
5. Benchrifa, M.; Mabrouki, J.; Elouardi, M.; et al. Detailed Study of Dimensioning and Simulating a Grid-Connected PV Power Station and Analysis of Its Environmental and Economic Effect, Case Study. *Model. Earth Syst. Environ.* **2023**, *9*, 53–61. [CrossRef]
6. Panagoda, L.P.S.S.; Sandeepa, R.A.H.T.; Perera, W.A.V.T.; et al. Advancements in Photovoltaic (Pv) Technology for Solar Energy Generation. *J. Res. Technol. Eng.* **2023**, *4*, 30–72. [CrossRef]
7. Maalouf, A.; Okoroafor, T.; Jehl, Z.; et al. A Comprehensive Review on Life Cycle Assessment of Commercial and Emerging Thin-Film Solar Cell Systems. *Renew. Sustain. Energy Rev.* **2023**, *186*, 113652. [CrossRef]
8. Buonomenna, M. Inorganic Thin-Film Solar Cells: Challenges at the Terawatt-Scale. *Symmetry* **2023**, *15*, 1718. [CrossRef]
9. Bonomo, P.; Frontini, F.; Loonen, R.; et al. Reinders, Comprehensive Review and State of Play in the Use of Photovoltaics in Buildings. *Energy Build.* **2024**, *323*, 114737. [CrossRef]
10. Taşer, A.; Koyunbaba, B.K.; Kazanasmaz, T. Thermal, Daylight, and Energy Potential of Building-integrated Photovoltaic (BIPV) Systems: A Comprehensive Review of Effects and Developments. *Sol. Energy* **2023**, *251*, 171–196. [CrossRef]

11. Chen, S.; Fu, Y.; Ishaq, M.; et al. Carrier Recombination Suppression and Transport Enhancement Enable High-Performance Self-Powered Broadband Sb_2Se_3 Photodetectors. *InfoMat* **2023**, *5*, e124000. [CrossRef]
12. Shahbaz, I.; Tahir, M.; Li, L.; et al. Advancements in 2D Transition Metal Dichalcogenides (TMDs) Inks for Printed Optoelectronics: A Comprehensive Review. *Mater. Today* **2024**, *77*, 142–184. [CrossRef]
13. Berni, A.; García-Guzmán, J.J.; Alcántara, R.; et al. Rapid and Eco-Friendly Ultrasonic Exfoliation of Transition Metal Dichalcogenides Supported on Sonogel-Nanocarbon Black: A Non-Precious Electrocatalyst for Hydrogen Evolution Reaction. *Int. J. Hydrogen Energy* **2024**, *90*, 690–700. [CrossRef]
14. Li, R.; Liu, X.; Chen, J. Opportunities and Challenges of Hole Transport Materials for High-Performance Inverted Hybrid-Perovskite Solar Cells. *Exploration* **2023**, *3*, 20220027. [CrossRef]
15. Park, J.H.; Hwang, S.K.; Ji, S.G.; et al. Characterization of Various Tandem Solar Cells: Protocols, Issues, and Precautions. *Exploration* **2023**, *3*, 20220029. [CrossRef]
16. Khan, M.A.; Johora, F.T.A.; Asad, A.; et al. Effect of Defect Density Variation in CdTe Solar Cell Using Cu as A Hole Transport Layer and Back Contact. *IJEEAS* **2024**, *7*. [CrossRef]
17. Bahadur, A.; Saeed, A.; Iqbal, S.; et al. Morphological and Magnetic Properties of BaFe12O19 Nanoferrite: A Promising Microwave Absorbing Material. *Ceram. Int.* **2017**, *43*, 7346–7350. [CrossRef]
18. Shimul, A.I.; Khan, M.A.; Rayhan, A.; et al. Machine Learning-Based Optimization and Performance Enhancement of $CH_3NH_3SnBr_3$ Perovskite Solar Cells with Different Charge Transport Materials Using SCAPS-1D and wxAMPS. *Adv. Theory Simul.* **2025**, *2500182*. [CrossRef]
19. Sajid, M.; Qamar, M.A.; Farhan, A.; et al. Emerging Paradigms in Two-Dimensional Materials: Classification, Synthesis, and the Role of Defects in Electrocatalysis for Water Splitting and Oxygen Reduction Reaction. *J. Environ. Chem. Eng.* **2024**, *12*, 113784. [CrossRef]
20. Shreya; Phogat, P.; Jha, R.; et al. Emerging Advances and Future Prospects of Two Dimensional Nanomaterials Based Solar Cells. *J. Alloys Compd.* **2024**, *1001*, 175063. [CrossRef]
21. Farag, A.A.M.; Roushdy, N.; Badran, A.-S.; et al. A Comprehensive Investigation of the Synthesis, Spectral, DFT, and Optical Properties of a Novel Oxadiazolyl-Pyrano[3,2-*c*]Quinoline for Photosensor Applications. *J. Mol. Struct.* **2024**, *1318*, 139387. [CrossRef]
22. Li, S.; Xu, M.; Guo, Z.; et al. High Current Density Heterojunction Bipolar Transistors with 3D-GaN/2D-WSe_2 as Emitter Junctions. *Mater. Horiz.* **2024**. [CrossRef]
23. Aftab, S.; Goud, B.S.; Mukhtar M.; et al. Perovskite Photovoltaics with Cutting-Edge Strategies in 2D TMDs-Based Interfacial Layer Optimization. *Mater. Today Sustainability* **2024**, *28*, 100982. [CrossRef]
24. Tiwari, P.; Patel, K.; Krishnia, L.; et al. Potential Application of Multilayer N-Type Tungsten Diselenide (WSe_2) Sheet as Transparent Conducting Electrode in Silicon Heterojunction Solar Cell. *Comput. Mater. Sci.* **2017**, *136*, 102–108. [CrossRef]
25. Gautam, S.; Patel, A.K.; Mishra, R.; et al. Performance Analysis of WSe_2 Solar Cell with Cu_2O Hole Transport Layer by Optimization of Electrical and Optical Properties. *J. Comput. Electron.* **2022**, *21*, 1373–1385. [CrossRef]
26. Wei, M.; Xiao, K.; Walters, G.; et al. Combining Efficiency and Stability in Mixed Tin–Lead Perovskite Solar Cells by Capping Grains with an Ultrathin 2D Layer. *Adv. Mater.* **2020**, *32*, 1907058. [CrossRef]
27. Zhang, W.; Guo, X.; Cui, Z.; et al. Strategies for Improving Efficiency and Stability of Inverted Perovskite Solar Cells. *Adv. Mater.* **2024**, *36*, 2311025. [CrossRef]
28. Rayhan, A.; Khan, M. A.; Islam, R. Enhancing $CsSn_{0.5}Ge_{0.5}I_3$ Perovskite Solar Cell Performance via Cu_2O Hole Transport Layer Integration. *Int. J. Photoenergy* **2024**. [CrossRef]
29. Li, Z. SNU Open Repository and Archive: Study of Cu_2O Thin Film Transistor and Oxide Semiconductor Negative Differential Transconductance Device for Logic Circuits. PhD thesis, Seoul National University, Seoul, Korea. (In Korean) [CrossRef]
30. Kotnala, R.K.; Kaushik, A.S.; Subramanian, S.S.; et al. Advanced Functional Materials for Sustainable Environments; Springer Nature: New York, NY, USA, 2024.
31. Xie, W.; Du, C.; Ding, Y.; et al. Numerical Investigation on the Performance of Heterojunction Solar Cells with Cu_2O as the Hole Transport Layer and Cu_2MoSnS_4 as the Absorption Layer. *Phys. Lett. A* **2024**, *528*, 130029. [CrossRef]
32. Kumar, V.; Masudy-Panah, S.; Tan, C.C.; et al. Copper Oxide Based Low Cost Thin Film Solar cells. In Proceedings of the 2013 IEEE 5th International Nanoelectronics Conference (INEC), Singapore, 2013. [CrossRef]
33. Yang, R.; Zhang, X.; Chen, B.; et al. Tunable Backbone-Degradable Robust Tissue Adhesives via in Situ Radical Ring-Opening Polymerization. *Nat. Commun.* **2023**, *14*, 6063. [CrossRef]
34. Zhang, H.; Chang, J.; Zhang, R.; et al. Enhanced Sub-ppm NO_2-Sensing Properties of SnS_2 Sheet Flowers Deco-

rated with Au Nanoparticles at Near Room Temperature. *IEEE Sens. J.* **2022**, *22*, 22127–22133. [CrossRef]
35. Li, M.; Gao, X.; Zhang, Y.; et al. Ammonia Sensing Properties of SnS_2/SnO_2 Nanocomposite-Based Gas Sensor by SnS_2 Annealing. *IEEE Sens. J.* **2022**, *22*, 23456–23463. [CrossRef]
36. Gedi, S.; Reddy, V.R.M.; Pejjai, B.; et al. A Facile Inexpensive Route for SnS Thin Film Solar Cells with SnS_2 Buffer. *Appl. Surf. Sci.* **2016**, *372*, 116–124. [CrossRef]
37. Yao, K.; Shan, S.; Jia, Q. One-step Synthesis of Urchinlike SnS/SnS_2 Heterostructures with Superior Visible-Light Photocatalytic Performance. *Catal. Commun.* **2017**, *101*, 51–56. [CrossRef]
38. Mahmud, S.T.; Mia, R.; Mahmud, S.; et al. Recent Developments of Tin (II) Sulfide/Carbon Composites for Achieving High-Performance Lithium Ion Batteries: A Critical Review. *Nanomaterials* **2022**, *12*, 1246. [CrossRef]
39. Anucha, C. B.; Altin, I.; Bacaksiz, E.; et al. Titanium Dioxide (TiO_2)-Based Photocatalyst Materials Activity Enhancement for Contaminants of Emerging Concern (CECs) Degradation: In the Light of Modification Strategies. *Chem. Eng. J. Adv.* **2022**, *10*, 100262. [CrossRef]
40. Cao, Y.; Li, S.; Lv, C.; et al. Experimental Demonstration of Angle-Dependent GMR Effect in $Py/WSe_2/Co$ Spin Valve Structure. *IEEE Trans. Electron. Dev.* **2021**, *68*, 3690–3695. [CrossRef]
41. Wang, Y.; Fang, X.; Sun, L. Enhanced Responsivity of WSe_2 Phototransistor Using Au Nanoparticles. In Proceedings of the International Conference on Optoelectronic Materials and Devices (ICOMD 2024), Chongqing, China, March 2025. [CrossRef]
42. Sharma, A.; Varshney, U.; Gupta, G. Light Stimulation Enhanced Detection of NO at ppb-Level at Room Temperature Using $MoS_2/WSe_2/GaN$ Heterostructure Sensor. *J. Mater. Chem. A* **2025**, *13*, 8484–8496. [CrossRef]
43. Kasi, G.; Thanakkasaranee, S.; Stalin, N.; et al. Enhancement of Antimicrobial Properties and Cytocompatibility Through Silver and Magnesium Doping Strategies on Copper Oxide Nanocomposites. *J. Alloys Compd* **2024**, *1007*, 176481. [CrossRef]
44. Maslov, A.D.; Litvinov, V.G.; Ermachikhin, A.V.; et al. Investigation of Recombination Centers in the Active Layers of HIT Solar Cells. In Proceedings of the 2020 ELEKTRO, Taormina, Italy, 2020. [CrossRef]
45. Chen, M.; Ishaq, M.; Ren, D.; et al. Interface Optimization and Defects Suppression via NaF Introduction Enable Efficient Flexible Sb_2Se_3 Thin-Film Solar Cells. *J. Energy Chem.* **2024**, *90*, 165–175. [CrossRef]
46. Li, F.; Jen, A.K.-Y. Interface Engineering in Solution-Processed Thin-Film Solar Cells. *Acc. Mater. Res.* **2022**, *3*, 272–282. [CrossRef]
47. Ma, S.; Du, D.X.; Gao, C.; et al. Improving the Performance of Industrial TOPCon Solar Cells Through the Insertion of Intrinsic a-Si Layer. *Sol. Energy Mater. Sol. Cells* **2024**, *275*, 113024. [CrossRef]
48. Liu, Y.; Qin, H.; Peng, C.; et al. Boosting the Responsivity of Amorphous-Ga2O3 Solar-Blind Photodetector via Organosilicon Surface Passivation. *Appl. Phys. Lett.* **2024**, *124*, 082102. [CrossRef]
49. Li, W.; Wang, G.; Long, Y.; et al. BCP Buffer Layer Enables Efficient and Stable Dopant-Free P3HT Perovskite Solar Cells. *ACS Appl. Mater. Interfaces* **2024**, *16*, 63019–63025. [CrossRef]
50. Mohamad Noh, M.F.; Arzaee, N.A.; Fat, C.C.; et al. Perovskite/CIGS Tandem Solar Cells: Progressive Advances from Technical Perspectives. *Mater. Today Energy* **2024**, *39*, 101473. [CrossRef]
51. Rawat, S.; Gupta, R.; Gohri, S. Performance Assessment of CIGS Solar Cell with Different CIGS Grading Profile. *Mater. Today Proc.* **2023**, S2214785323014025. [CrossRef]
52. Bai, H.; Qian, G.; Liang, Q.; et al. Tuning Electronic and Optical Properties of Two-Dimensional Vertical van der Waals Blue Phosphorene/SnS_2 Heterostructure by Strain and Electric Field. *Comput. Mater. Sci.* **2024**, *238*, 112948. [CrossRef]
53. Zhou, Y.; Mu, H.; Zhang, C.; et al. SnS_2/WSe_2 van der Waals Single-Detector Spectrometer with a Dynamically Selecting Spectral Reconstruction Strategy. *IEEE Electron. Dev. Lett.* **2025**, *1*. [CrossRef]
54. Haque, M.D.; Ali, M.H.; Islam, A.Z.M.T. Efficiency Enhancement of WSe_2 Heterojunction Solar Cell with CuSCN as a Hole Transport Layer: A Numerical Simulation Approach. *Sol. Energy* **2021**, *230*, 528–537. [CrossRef]